Structures 59 (2024) 105699

Contents lists available at ScienceDirect

Structures

journal homepage: www.elsevier.com/locate/structures

Layout and geometry optimization design for 3D printing of self-supporting structures

Jun Ye [a,e], Xiaoyang Lin [a,b], Hongjia Lu [c,*], Hongyao Shen [d], Zhen Wang [f,*], Yang Zhao [a,*]

[a] College of Civil Engineering and Architecture, Zhejiang University, Hangzhou 310058, China
[b] Center for Balance Architecture, Zhejiang University, Hangzhou 310014, China
[c] Centre for Innovative Structures and Materials, RMIT University, Melbourne 3001, Australia
[d] The State Key Laboratory of Fluid Power and Mechatronic Systems, College of Mechanical Engineering, Zhejiang University, Hangzhou 310027, China
[e] School of Civil Engineering, University of Leeds, Leeds LS2 9JT, UK
[f] Department of Civil Engineering, Hangzhou City University, Hangzhou 310015, China

ARTICLE INFO

Keywords:
Self-supporting structure
Layout optimization
Geometry optimization
Manufacturing constraints
3D printing

ABSTRACT

As the demand for high-performance structures in various scenarios continues to rise, the complexity of engineering structures also increases, necessitating the development of advanced design methods and the additive manufacturing (AM) of sophisticated structures. While the layout optimization method based on the ground structure technique can produce optimized designs, the gravity-induced overhang effect during the printing process often requires additional support materials. The use of additional support materials during the printing process can result in higher material costs or the need for post-processing to remove the support structures, significantly hindering the adoption of AM in practice. This paper presents an optimization framework to obtain self-support optimization designs and provides a practical validation for the effectiveness of the proposed framework. Firstly, a self-support point-line structure is obtained via the layout and geometry optimization, considering overhang constraints. Secondly, the point-line structure is transformed into a physical model with nodal expansion considered (i.e., taking into account the overlapping of members at nodes). Finally, the physical models are sliced and printed using both a plastic Fused Deposition Modeling (FDM) printer and a metal Wire Arc Additive Manufacturing (WAAM) printer. The results confirm that the proposed process is effective for both plastic and metal printing, demonstrating its exceptional versatility.

1. Introduction

Topology optimization is a long-established approach in structural design that aims to determine the optimal layout of structural elements within a given design domain, subject to various performance and design constraints. While the optimized structures produced by this approach often have high performance, their free-form shapes can make them challenging to manufacture using traditional manufacturing methods. As a result, the use of additive manufacturing (AM) techniques is frequently considered in the design of topology-optimized structures, and the joint study of AM and topology optimization has been an active area of research.

AM technology enables the manufacturing of freeform structures through the accumulation of material layer by layer [1]. In the field of steel structures, metal AM technology has already been used in industrial projects (Fig. 1) such as the AM footbridge made by MX3D in the Amsterdam [2] and the small footbridge at TU Darmstadt [3]. In order to better utilize the potential of metallic AM technology in structural engineering, extensive research has been carried out on analysing the mechanical properties of metal AM materials, joints and other structural components [4]. In terms of metal AM materials, the mechanical properties and fatigue properties of wire arc additively manufactured (WAAM) steel, high-strength steel, and stainless steel have been investigated through experiments [5–9]. Huang et al. [10] has made excellent work by proposing an intrinsic model of WAAM steel, which is able to predict the full stress-strain curve of WAAM steel. In terms of nodes, bolted connections are the most commonly used connections in steel structures. The mechanical properties of single lap shear and double lap shear WAAM steel bolted connections are investigated experimentally and compared with the design codes for conventional

* Corresponding authors.
E-mail addresses: j.ye2@leeds.ac.uk (J. Ye), hongjia.lu@rmit.edu.au (H. Lu), wangzhen@hzcu.edu.cn (Z. Wang), ceyzhao@zju.edu.cn (Y. Zhao).

https://doi.org/10.1016/j.istruc.2023.105699
Received 5 May 2023; Received in revised form 19 November 2023; Accepted 2 December 2023
Available online 13 December 2023

(a) AM footbridge in Amsterdam [2] (b) AM footbridge at TU Darmstadt [3]

Fig. 1. Construction projects made by WAAM.

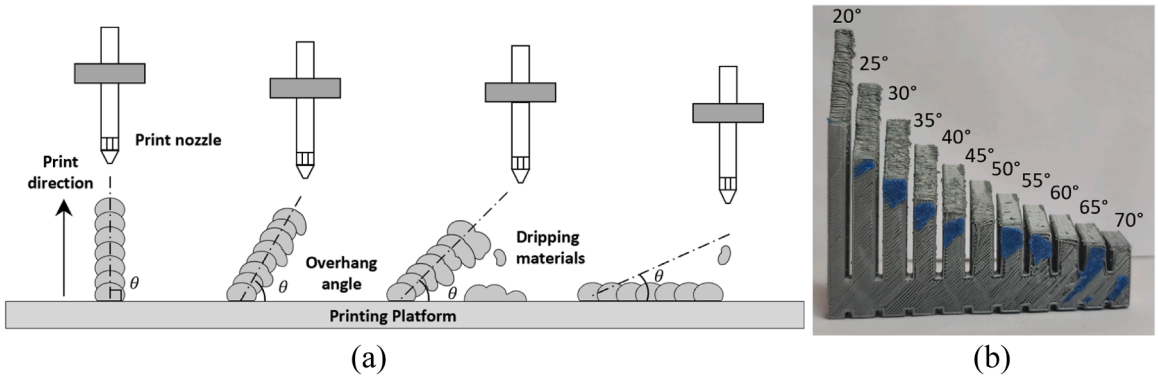

Fig. 2. Effect of overhang angle on print quality: (a) schematic; (b) printed model.

connections [11–13]. In addition, new AM steel connections for modular building systems are also attracting research interest [14]. In terms of components, there is extensive research on the mechanical properties of AM steel beams and columns with different cross-sectional shapes [15–17], as well as studies on the optimization of member [18–20]. While numerous studies have explored the applications of AM in engineering, the primary focus has often been on analysing the mechanical performance. However, addressing the overhang problem is a pivotal aspect in extending the real-world application of AM [21]. Due to the overhang problem, the print quality decreases as the overhang angle of the component decreases (Fig. 2). Material collapse can occur when the overhang angle is too small, resulting in the failure of material deposition. Therefore, the overhang angle of the structural component needs to be greater than the minimum allowable self-supporting angle of the printing material. Note that the minimum allowable self-supporting angle is dependent on the printing material and AM configurations.

There are two main approaches within topology optimization: discrete truss optimization and continuum topology optimization. While discrete truss optimization uses point-line model to discretize the design domain, the continuum topology optimization uses finite element discretization. In this study, we focus on the former, which involves optimizing the layout of discrete structural elements such as trusses or beams. One of the pioneering methods for discrete structure topology optimization is layout optimization based on the ground structure proposed by Dorn et al. [22]. However, this approach is computationally expensive for large-scale structural design problems. To address this issue, Gilbert et al. [23] proposed an iterative scheme that uses a sparsely connected ground structure in the first iteration and gradually adds members to it in the subsequent iterations so that size of the optimization matrix of each iteration is reduced compared to the full ground structure problem. Despite its efficiency, the optimization results from the layout optimization process can still be structurally complex, with a large number of members and nodes, which can hinder practical applications. To address this issue, Parkes [24] introduced the "joint cost" concept in 1975, which penalized short members in the objective function to simplify the structural layout during optimization. He et al. [25] developed a geometry optimization method that used node movement and member filtering to rationalize optimized layouts. Smith et al. [26] performed load tests on layout-optimized structures fabricated by metal 3D printing, and the effectiveness of the fabrication process as well as the mechanical properties of the optimized structures were verified. Ye et al. [27] proposed an optimization framework for generating optimized tubular truss structures suitable for metal 3D printing. This framework combines layout, geometry, and cross-sectional optimization, considering multiple load cases and enabling significant material savings for metal 3D printing. Liu et al. [28] proposed a truss structure layout optimization method considering modularization constraints, and the optimization results contain a variety of repetitive modules. However, the above optimization methods and commonly used commercial optimization methods, do not consider manufacturing constraints of truss structures.

A common way to deal with this manufacturing constraint is to add supporting structures under the overhang parts. However, for metal printing, the addition of supporting structures during the 3D printing process can result in increased material costs, reduced printing efficiency, and difficulties in removing the support [29]. Another way to solve the problem of overhang effects is to design self-supporting structures. Some researchers have explored strategies to generate self-supporting structures by introducing overhang constraints in topology optimization, including methods such as wedge-shaped spatial filter [30–32], density gradient information [33], level set [34], and so on [35,36]. But the current research in this area mainly focuses on continuum structure optimization. In discrete structure optimization, He et al. (2019) have proposed an approach to obtaining self-supporting structures by considering overhang constraints in the layout and geometry optimization process [37]. However, the studies on the

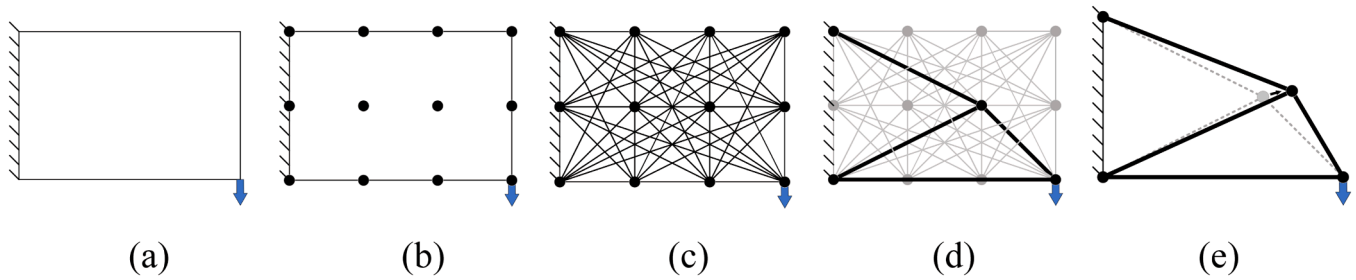

Fig. 3. Steps in the optimization: (a) assign the design domain, load, and supports; (b) discretize the domain into a node grid; (c) generate ground structure; (d) solve the layout optimization problem and get the optimal layout; (e) identifying optimized nodal positions in geometry optimization.

optimization of self-supporting truss structures for 3D printing are still very limited and there is a lack of experimental validations on the proposed algorithm.

Therefore, this paper combines the previous approaches and proposes an end-to-end pilot line for obtaining self-support optimized structures, and the effect of material characteristics and printing parameters on printing is considered through the adjustable parameter of minimum allowable overhang angle. The members that do not satisfy the overhang constraints are removed in the layout optimization stage. Then the inclined angle of the members is constrained during the geometry optimization. The method considers manufacturing constraints in both the layout and geometry optimization procedures and the effectiveness of the algorithm is verified by printing examples based on both FDM and WAAM.

2. Layout and geometry optimization

Layout optimization includes mainly four steps, as shown in Fig. 3. Firstly, the design domain boundary and loading conditions are defined, as shown in Fig. 3(a). Secondly, the design domain is discretized by grid nodes, as demonstrated in Fig. 3(b). Then, the grid nodes are connected and the ground structure is generated as shown in Fig. 3(c). Finally, the layout optimization problem is solved and the optimal structure layout is obtained, as shown in Fig. 3(d). This problem is a linear programming problem and the mathematical model can be expressed as follows:

$$\min \quad V = \mathbf{l}^{\mathrm{T}}\mathbf{a} \tag{1a}$$

$$\text{s.t.}\mathbf{B}\mathbf{q}_{\alpha} = \mathbf{f}_{\alpha} \tag{1b}$$

$$-\sigma^{-}\mathbf{a} \le \mathbf{q}_{\alpha} \le \sigma^{+}\mathbf{a} \tag{1c}$$

$$\mathbf{a} \ge 0, \tag{1d}$$

where: $\mathbf{a} = [a_1, a_2, \ldots, a_m]^T$ is the member cross-section area vector with m donating the number of members; $\mathbf{q} = [q_1, q_2, \ldots, q_m]^T$ is the internal force vector; V is the total volume of the structure; $\mathbf{l} = [l_1, l_2, \ldots, l_m]^T$ is the member length vector; $\mathbf{B}$ is the equilibrium matrix containing the direction of the component. $\mathbf{f}_{\alpha}$ is the nodal load vector for the load case numberα and σ^{-}, σ^{+} denote the ultimate strength of the material in compression and tension, respectively.

The design variables are member cross-section areas $\mathbf{a}$ and internal forces of the member $\mathbf{q}$. Eq. 1(a) is the objective of minimum total truss volume, Eq. 1(b) is the equilibrium constraint, and Eq. 1(c) denotes the material strength constraint.

The results from layout optimization may involve complex geometries that are difficult for manufacturing and practical application. Therefore, to further rationalize the optimized structures obtained from layout optimization, geometry optimization is conducted. In this step, the nodal positions are treated as additional optimization variables to allow the joints to move around, as shown in Fig. 3(e). Consequently, the problem is a non-linear non-convex optimization problem, and its mathematical model can be expressed as follows:

$$\min \quad V = \mathbf{l}(\mathbf{x}, \mathbf{y}, \mathbf{z})^{\mathrm{T}}\mathbf{a} \tag{2a}$$

$$\text{s.t.}\mathbf{B}(\mathbf{x}, \mathbf{y}, \mathbf{z})\mathbf{q}_{\alpha} = \mathbf{f}_{\alpha} \tag{2b}$$

$$-\sigma^{-}\mathbf{a} \le \mathbf{q}_{\alpha} \le \sigma^{+}\mathbf{a} \tag{2c}$$

$$\mathrm{x}^{\mathrm{ub}} \ge \mathbf{x} \ge \mathbf{x}^{\mathrm{lb}} \tag{2d}$$

$$\mathrm{y}^{\mathrm{ub}} \ge \mathbf{y} \ge \mathbf{y}^{\mathrm{lb}} \tag{2e}$$

$$\mathrm{z}^{\mathrm{ub}} \ge \mathbf{z} \ge \mathbf{z}^{\mathrm{lb}} \tag{2f}$$

$$\mathbf{a} \ge 0 \tag{2g}$$

$$\sin\theta_{\min} - \left|\frac{X_i d_x}{l_i} + \frac{Y_i d_y}{l_i} + \frac{Z_i d_z}{l_i}\right| \le 0, \tag{2h}$$

where: X_i, Y_i, Z_i are the projection of the length l_i of the ith member in the x, y, z axis directions in the global cartesian coordinate system, respectively. The projection can be calculated as $X_i = x_2 - x_1, Y_i = y_2 - y_1, Z_i = z_2 - z_1$; $\theta_{\min}$ is the minimum allowable self-supporting angle; d_x, d_y, d_z are the three components of the normalized building direction vector, where the building direction is set to be $(0, 0, 1)$ in the examples in this paper; $\mathrm{x}^{\mathrm{ub}}, \mathrm{x}^{\mathrm{lb}}$, $\mathrm{y}^{\mathrm{ub}}, \mathrm{y}^{\mathrm{lb}}, \mathrm{z}^{\mathrm{ub}}, \mathrm{z}^{\mathrm{lb}}$ are the upper and lower moving limits of the nodal positions. The other symbols in this geometry optimization model are defined in the layout optimization mathematical model shown in the defined equations.

In the geometry optimization model, the design variables are nodal position $(\mathbf{x}, \mathbf{y}, \mathbf{z})$, member cross-section area $\mathbf{a}$, and internal force $\mathbf{q}$ of the members. To ensure that the geometry optimization results do not deviate significantly from the theoretical optimum value, the node movement is restricted to the vicinity of the initial position. Eqs. 2(d)–2(f) represent the nodal movement constraints. Eq. 2(h) denotes the overhang constraint in the geometry optimization.

It is noted that the structural nodes cannot move outside of the design domain during the geometry optimization process. Line constraints and design domain constraints are therefore necessary to be taken into account. Certain nodes (e.g., on the supported boundary) are restricted to moving on the boundary by line constraint, while all the nodes are restricted to lying in the assigned design domain by design domain constraint. However, design domain constraints are only applied to the nodes that have the potential to move out of the design domain to improve the optimization efficiency.

In a 2D design domain, $T^x x + T^y y + T^c = 0$ represent a line, where T^x, T^y, T^c are three coefficients of the certain line. It can also be written in vector form: $Tv = 0$, where: $T = [T^x, T^y, T^c]$. Then the line constraint and design domain constraint of the i^{th} node can be described as (3) and (4):

$$T_i^L v_i = 0 \tag{3}$$

$$T_i^D v_i > 0 \tag{4}$$

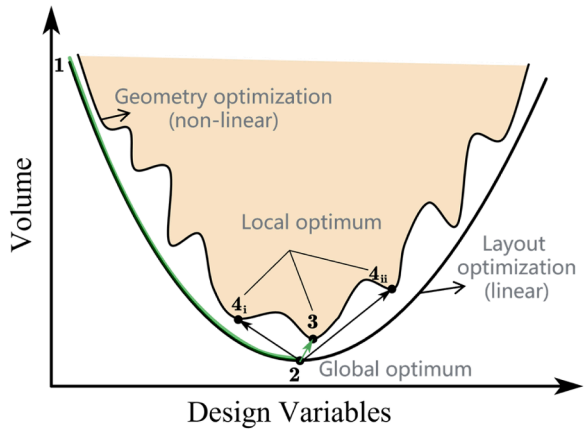

Fig. 4. Relation between volume and design variables.

where T_i^L represents the coefficient vector of the line that the ith node lies on and T_i^D represents the coefficient vectors of the boundary line that the ith node may cross. It is worth noting the importance of defining the normal direction of the lines when judging the relationship between node and boundary. Similarly, face and domain constraints for 3D design domains can also be derivated and applied in the design optimization process.

3. Optimization strategies considering overhang constraints

The optimization framework presented above mainly consists of layout optimization and geometry optimization methods. Since geometry optimization is a non-convex and non-linear optimization problem, the quality of the optimized solution is significantly influenced by the initial starting point provided. Due to this reason, the optimal solution from the traditional layout optimization is utilized in the first step to provide a good starting point for geometry optimization (point 2 in Fig. 4). Then in the second step, the geometry optimization (Formulation (2)) along with geometry modifications such as node merging and component deletion are carried out, considering multiple constraints to obtain near-optimal solution (point 3 in Fig. 4, not points 4_i and 4_{ii}). This two-step optimization algorithm significantly improved efficiency compared to traditional methods. When the layout optimization mesh density is low, geometry optimization with moveable nodes can even yield better results.

To ensure that the optimization results are printable, the overhang angle of the components needs to be constrained in both the layout and geometry optimization process. For this, we generally follow the approach in [29]. The optimization strategy is described as below, and the flow chart is shown in Fig. 5.

3.1. Layout optimization

Before the layout optimization begins, conditions such as design domain size, material tensile strength, load cases, and boundary constraints are set in a Python-based program. Parameters such as mesh density, initial ground structure component length thresholds, minimum allowable self-supporting angle, and building direction are also specified in the program. The procedures are described below:

Firstly, discretize the design domain and establish the minimum connected ground structures. Only the structural elements with a length less than the threshold will be activated. The remaining components are considered as potential member sets to be added in subsequent iterations.

Secondly, the unprintable members in both the ground structures and potential member-adding sets will be removed. The member is considered printable if its overhang angle is greater than the minimum allowable self-supporting angle, as shown in Fig. 6, and Eq. 2 (h) is used as the criterion for judgement. This method is used to remove members that do not meet the criterion from the initial ground structure and potential member sets to avoid unprintable members appearing in the subsequent optimization process. When the number of connectable members in the initial ground structure is small, the equilibrium matrix

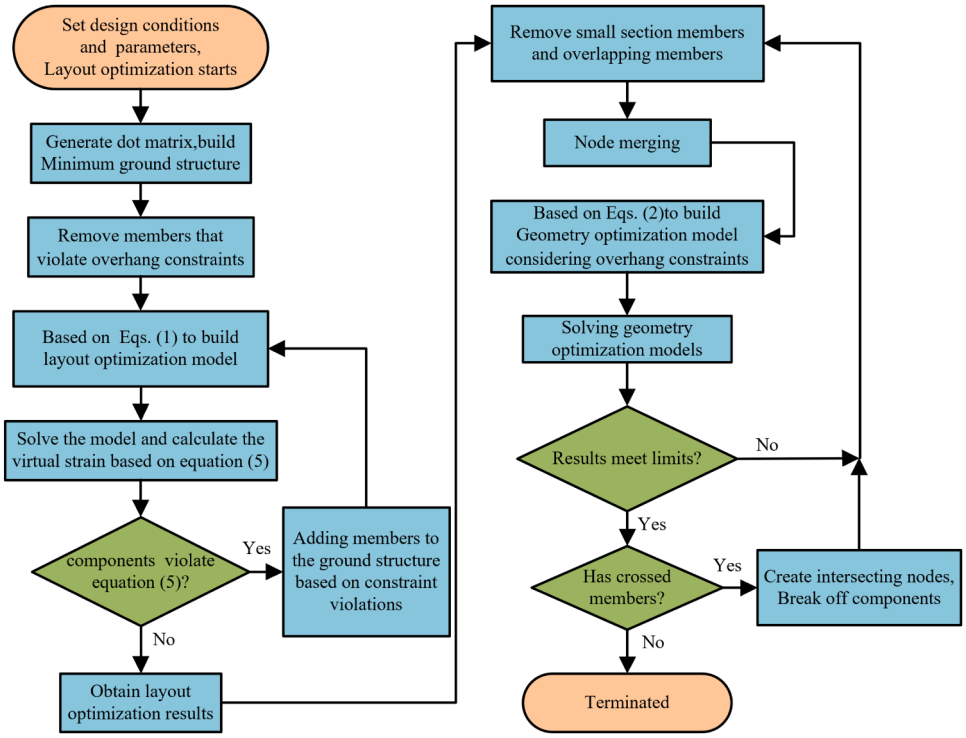

Fig. 5. Flow chart of the proposed optimization method.

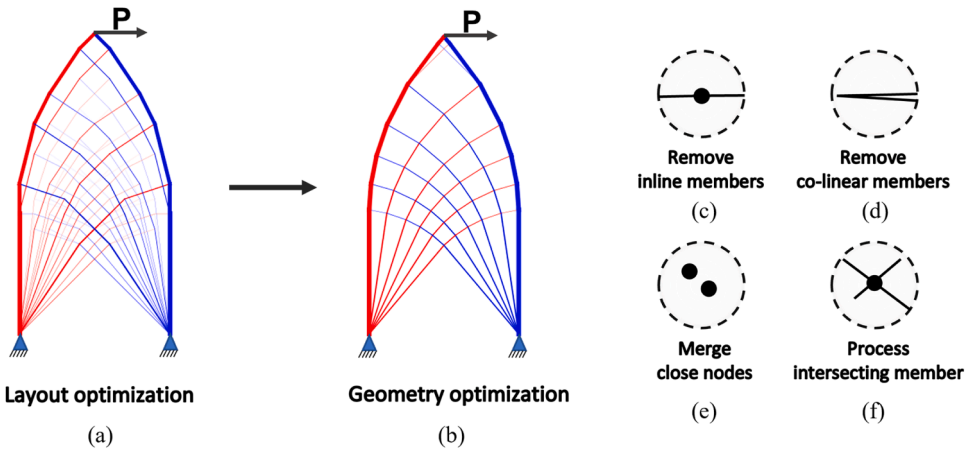

Fig. 7. Process and operations in geometry optimization.

may appear to be unsolvable. In this case, by increasing the initial ground structure member length threshold or mesh density, a sufficient number of members can be ensured in the initial ground structures for a solution to be obtained. In this study, the member length thresholds vary in relation to the initial grid spacing, with multipliers of 1.733, 2, 3, 3 and 4 corresponding to minimum allowable self-supporting angles of 0°, 30°, 40°, 50°, and 60°, respectively.

In the third step, the layout optimization model based on the "member adding technique" [23] will be established. According to the mathematical model of layout optimization, the optimization variables are selected, and the functions are created based on the minimum volume objective function. Design constraints such as mechanical equilibrium and material strengths are taken into account. The layout-optimized dual model is derived from Eq. (1). When the relative displacements and lengths of the ith member are u_i and l_i respectively, it is known from Michell optimization theory [38] that the virtual strain of the member of the optimal structure should satisfy:

$$-\frac{1}{\sigma^-} \le \frac{\boldsymbol{u}_i}{\boldsymbol{l}_i} \le \frac{1}{\sigma^+} \tag{5}$$

Finally, Eq. (5) is used as the criterion for the potential member-adding process, and it is taken into account in the iterative solution process. In each iteration of the member adding method, potential members that violate constraint (5) need to be added to the ground structure. For large-scale problems, the step-by-step method of adding members is more efficient compared to adding all violated members in only one step. Therefore, all the potential members are firstly sorted in descending order based on their K^{add} values, and then the members associated with the lowest 5% K^{add} values are added to the ground structure for carrying out the layout optimization in the next iteration [23]. The optimization model is solved again until the virtual strains of all members satisfy Eq. (5), and K^{add} is the number of members to be added.

3.2. Geometry optimization

Although the optimized layout structure is near theoretically optimal, the complex structural layout makes it difficult to be applied in practice (Fig. 7(a)). Therefore, the structural layout needs to be simplified through operations such as component merging and node fusion in geometry optimization, but they will not increase the material weight significantly [25], as shown in Fig. 7(b).

Firstly, the layout optimization result is extracted, and filtering thresholds are set to remove the members with small areas based on the layout optimization results. The inline and co-linear members appearing in the layout optimization process are also removed to obtain the initial solution for geometry optimization, as demonstrated in Fig. 7(c)~(d). In this study, when the radian value of the angle between the bars is less than 0.1, they are considered to be co-linear.

In the second step, the node merging strategy will be used to reduce the node number (Fig. 7(e)). By defining the node merging threshold R_s, nodes are grouped and merged to the centre of each group, as shown in Fig. 8. In this way, the structural nodes that are too close to each other will be merged and the optimized structure can be significantly simplified. By combining the iterative optimization strategy and node merging pre-processing before each optimization iteration, the efficiency of the

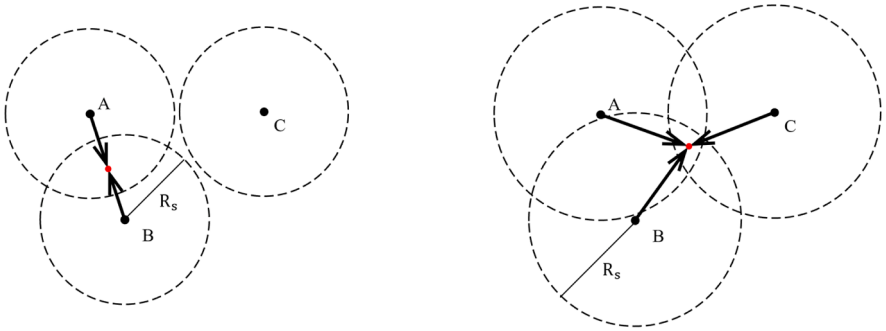

(a) When node merging threshold R_s is small, nodes A and B participate in the merging.

(b) When R_s is large, nodes A, B and C all participate in the merging.

Fig. 8. The effect of thresholds on node merging.

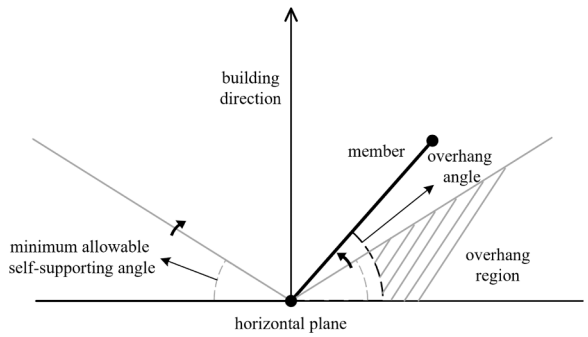

Fig. 6. Overhang angle and minimum allowable self-supporting angle.

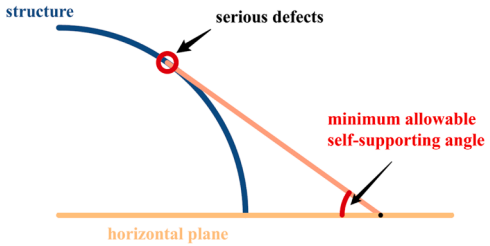

Fig. 9. Selection of minimum allowable self-supporting angle.

non-linear programming algorithm can be significantly improved. Here, R_s is set to 0.25 times the initial grid spacing.

In the third step, the geometry optimization model considering overhang constraints will be set up. Although the results extracted from the layout optimization can satisfy the overhang constraints, the nodes may violate the overhang constraints during the optimization process. This is because the nodes are movable in the geometry optimization process, it is necessary to apply overhang constraints to the node coordinates at both ends of the component. The constraint enables the component to meet the overhang constraints during the optimization process so that the optimized structure can be printed. Each node needs to consider the overhang constraints of all connected members. According to the above constraints, the constraint functions and objective function are created (Eq. (2)), and the geometry optimization model is established.

Finally, process the intersecting members and output results. When the iterative optimization results meet the limits, detection of member intersections will be conducted, and new nodes are generated to split the original members into multiple members at the intersection points (Fig. 6(f)). Then geometry optimization will be conducted to update the structures. If the volume change is less than the set limit, the process of crossover succeeds, and the new result will be obtained. Otherwise, the original result will be the output. For 3D design domain with unidirectional force, geometry optimization may result in a planar structure. Due to considerations of out-of-plane stability of the structure, the appropriate output can be selected from multiple solutions during the iterative optimization process.

4. Numerical examples

Several numerical examples are included in this section to demonstrate the effectiveness of the optimization approach. The minimum allowable self-supporting angle is measured via 3D printing a trumpet-shaped digital model in Section 4.1. 3D truss structures are then optimized using the proposed framework in this paper. The optimized point-line structures are transformed into 3D solid models using the approach proposed in [26]. By considering the overlapping volume at the joint position, the nodes are designed with a sphere shape with an expanded radius. Additionally, the members are expanded at two ends in accordance with the nodal expansion.

4.1. Minimum allowable self-supporting angle of the printing material

A trumpet-shaped model was designed to measure the minimum allowable self-supporting angle of the printing material. This measured value was then set as the limit for member overhang angle in the optimization models to verify the proposed framework in this paper. In the digital model of the trumpet-shaped structure, a quarter arc serves as the sectional curve (see Fig. 9). This design results in a gradual variation of the overhang angle, ranging from 0° at the base to 90° at the top. The physical dimensions of the printed model include a bottom circle with 40 mm radius, a top circle with 80 mm radius, and a height of 40 mm. The minimum allowable self-supporting angle of the selected wire for 3D printing was therefore obtained by measuring the angle between the tangent line and the horizontal plane at the point where serious defects were observed during the printing process (Fig. 9). In this study, the printing parameters are as follows: (1) The layer height is 0.2 mm. (2) The fill density is 40%. (3) Print speed is 60 mm/s. (4) Printing temperature is 210 ℃. (5) The nozzle diameter is 0.4 mm. The test results showed that the minimum allowable self-supporting angle for the PLA material was approximately 40° (Fig. 10).

4.2. Example of a unidirectional centrally loaded vertical truss

The design domain of example 1 was a 40 mm × 40 mm× 100 mm cube. In the optimization process, a 4 × 4 × 10 node grid is employed for constructing the ground structure. A unidirectional horizontal load P = 10 N was applied at the top centre of the design domain. Pinned supports were applied at the corner points of the bottom face, and the node spacing was set to 1, as shown in Fig. 11(a). The tensile strength and compressive strength of the material were 20 N/mm^2 and the building direction was vertically upward, i.e., $(0,0,1)$. According to the minimum allowable self-supporting angle measured in Section 4.1, this

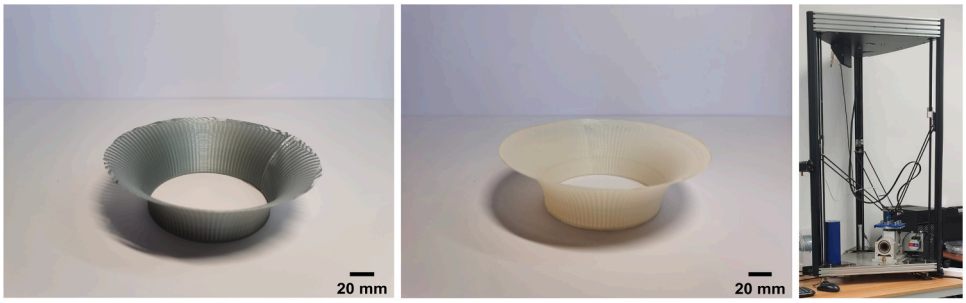

(a) Silver PLA (b) Skin PLA (c) 3D printer

Fig. 10. Minimum allowable self-supporting angle test for the trumpet-shaped model.

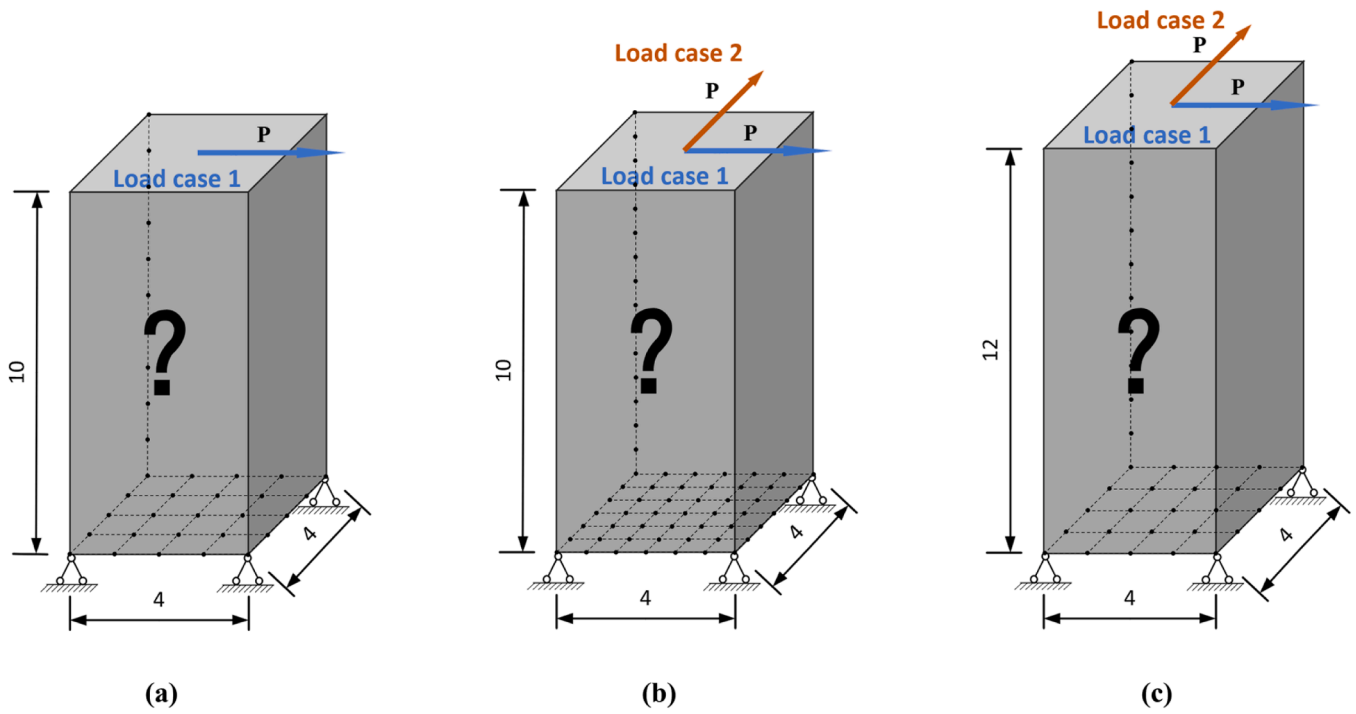

Fig. 11. (a) A load P = 10 N was applied at the top center of the 40 mm × 40 mm× 100 mm cubic design domain; (b) A load P = 10 N (arrows in orange and blue represent two load cases individually) was applied at the top center of the 40 mm × 40 mm× 100 mm cubic design domain; (c) A load P = 10 N (arrows in orange and blue represent two load cases individually) was applied at the top center of the 40 mm × 40 mm× 120 mm cubic design domain.

Table 1
Structural layout, geometry optimization, and printing test results considering allowable self-supporting angles (Example 1), where $\theta_{\min}$ denotes the minimum self-supporting angle.

$\theta_{\min}$	Layout optimization results	Geometry optimization results	Generated solid model	3D printing results
40°	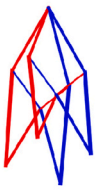			
50°	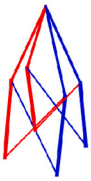	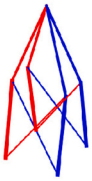	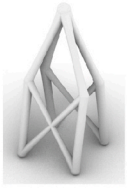	
60°	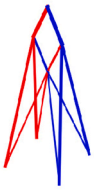	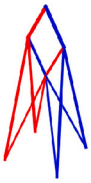		

Table 2
Structural layout, geometry optimization, and printing test results considering allowable self-supporting angles (Example 2), where $\theta_{\min}$ denotes the minimum self-supporting angle.

$\theta_{\min}$	Layout optimization results	Geometry optimization results	Generated solid model	3D printing results
40°	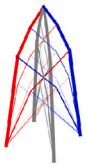	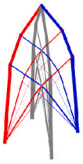	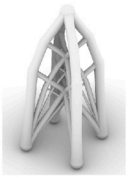	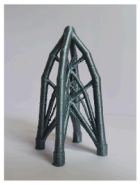
50°	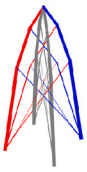	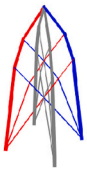	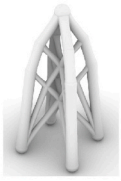	
60°	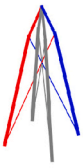	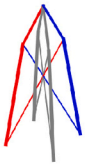	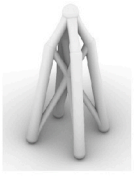	

Table 3
Structural layout, geometry optimization, and printing test results considering allowable self-supporting angles (Example 3), where $\theta_{\min}$ denotes the minimum self-supporting angle.

$\theta_{\min}$	0°	30°	40°	50°	60°
Layout optimization results	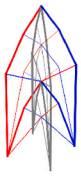	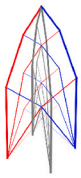	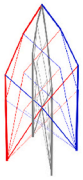	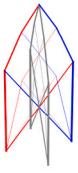	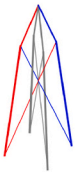
Geometry optimization results	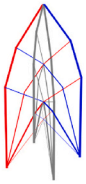	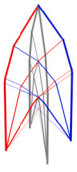	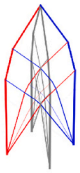	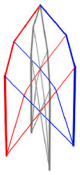	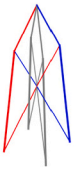
Generated solid model	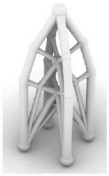		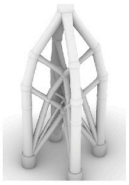	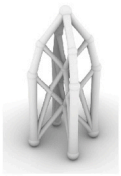	

parameter was set to 40°, 50°, and 60°, respectively, for comparison purposes. If the optimized structure with a 40-degree allowable self-supporting angle could be printed, the optimized structures with the other two allowable self-supporting angles could also be printed. The optimization results were therefore compared with each other to verify the effectiveness of the proposed optimization method. The structural layout and geometry optimization results for the three minimum allowable self-supporting angles are shown in Table 1, where members in red were in tension and blue members were in compression.

Table 4
Numerical results of optimization for different operating conditions and minimum allowable self-supporting angles.

Load case	Self-supporting angles (°)	The volume of layout optimization results (cm^3)	The volume of geometry optimization results (cm^3)	Volume increase for layout optimization caused by overhang constraint	Volume increase for geometry optimization caused by overhang constraint	Volume reduction after geometry optimization
Example 1	0	21.648	20.978	0.00%	0.00%	3.09%
	40	21.750	21.603	0.47%	2.98%	0.68%
	50	22.500	21.984	3.94%	4.79%	2.30%
	60	24.400	22.956	12.72%	9.43%	5.92%
Example 2	0	23.450	23.412	0.00%	0.00%	0.16%
	40	23.798	23.525	1.48%	0.49%	1.15%
	50	24.177	23.939	3.10%	2.25%	0.98%
	60	25.445	24.831	8.51%	6.06%	2.41%
Example 3	0	31.447	31.002	0.00%	0.00%	1.42%
	30	31.475	31.192	0.09%	0.62%	0.90%
	40	32.125	31.419	2.16%	1.34%	2.20%
	50	32.800	32.305	4.30%	4.20%	1.51%
	60	34.500	33.682	9.71%	8.65%	2.37%

4.3. *Example of a bi-directional centrally loaded vertical truss*

Example 2. set the grid density to be 1.5 based on Example 1, with a load P = 10 N applying at the top center of the 40 mm × 40 mm× 100 mm cubic design domain, as shown in Fig. 11 (b). Two load cases were considered as Example 2 was used to verify the applicability of the proposed optimization framework for multiple load cases. Layout and geometry optimization results for different minimum allowable self-supporting angles are shown in Table 2, where the grey color represents the members subjected to tension and compression under different load cases.

Example 3 sets the grid density the same as Example 1, with a load P = 10 N applying at the top center of the 40 mm × 40 mm× 120 mm cubic design domain, as shown in Fig. 11(c). Two load cases were considered. In Example 3, the minimum allowable self-supporting angle was set to be 0°, 30°, 40°, 50°, and 60° to verify the applicability of the

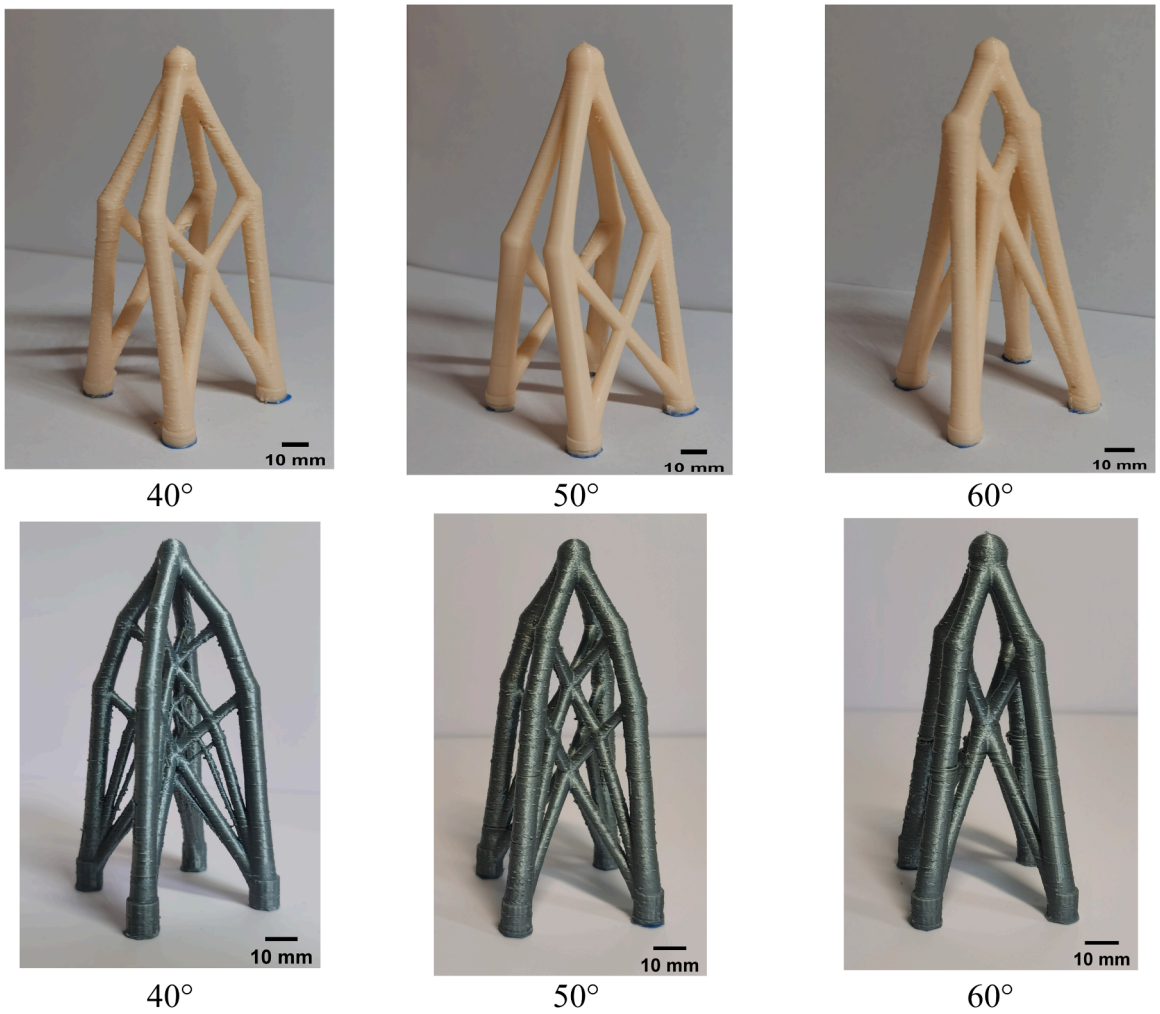

Fig. 12. Photo of printed models considering different minimum allowable self-supporting angles (top and bottom are Examples 1 and 2, respectively).

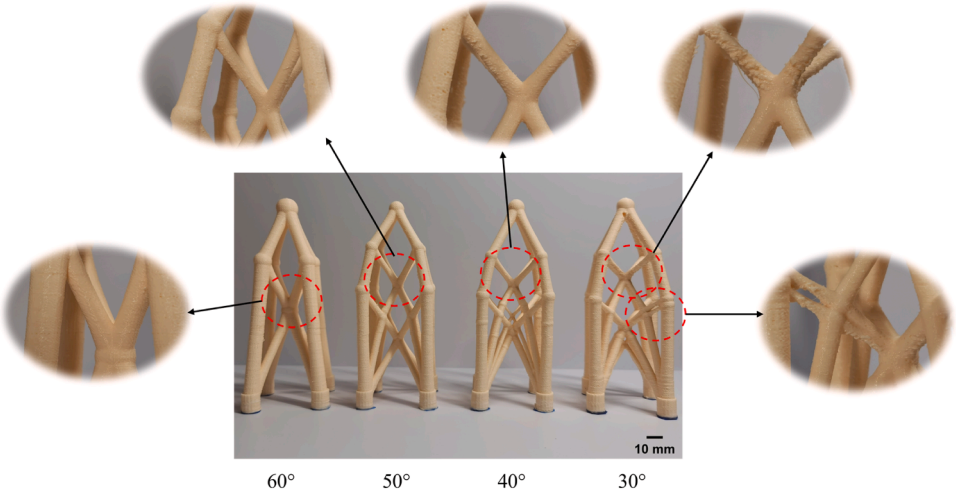

Fig. 13. Printed models of Example 3 considering different minimum allowable self-supporting angles as constraints.

proposed method for multiple load cases. Layout and geometry optimization results for different minimum allowable self-supporting angles are shown in Table 3.

4.4. Discussion on the numerical results

The layout optimization results and geometry optimization results can be robustly obtained using the proposed optimization framework considering structural performance and overhang manufacturing constraints, as shown in Table 4.

The optimization results in Table 4 show that the volumes after layout and geometry optimization tend to increase with the growing minimum allowable self-supporting angle set for different load cases. Compared with the layout optimization results, geometry optimization not only simplifies the layout of the structure and reduces the number of nodes but also has the possibility to further reduce the volume of the optimized structure due to the nodal movements. According to the minimum allowable self-supporting angle of the PLA material measured in this study, the maximum volume increase after considering manufacturing constraints is 2.98% in example 1. It is also shown in Table 4 that when the minimum allowable self-supporting angle is set to 50°, the maximum volume increase does not exceed 5% than the optimization results without manufacturing constraints, which illustrates the effectiveness of the proposed optimization framework.

5. Print validation with FDM

The data from the optimization results were extracted, including structural node positions, member connections, and cross-sectional areas. After the optimization process, 3D modeling was then carried out in commercially available Rhinoceros 7 software [39] to generate a solid model in STL format. The solid model was sliced, and print paths were generated using Repetier-Host software [40].

Examples were selected for 3D printing to verify the effectiveness of the proposed optimization framework. No material collapse was observed during the printing process of example 1 and Example 2, and the optimized structure could be successfully deposited with printing materials and the final results are shown in Fig. 12. It is clearly observed in the printing process of Example 3 that as the minimum allowable self-supporting angles decreases, the print quality of the component gradually decreases, as shown in Fig. 13. When the angle drops to 30 degrees, below the minimum allowable self-supporting angle of the PLA wire itself, the components inside the optimized structure can no longer be printed intact.

The results show that using a 3-axis 3D printer can successfully manufacture the optimized structures without additional supporting structures, which again illustrates the effectiveness of the optimization approach. In previous studies, the print quality of printed models is usually judged by visual inspection. Here, we propose the print loss rate φ to quantitatively assess the print quality of the members by comparing the theoretical cross-sectional area A_0 of the members in the model with the actual cross-sectional area A_i. The print loss rate of the nth member in the model is defined as $\varphi_n = (1 - \frac{A_n}{A_{0,n}})$, with larger value representing a poorer member print quality. The diameter values of each member are measured using a vernier caliper (with a maximum accuracy of $\pm$ 0.03 mm) at multiple sections along its length. The smallest measured diameter is then used to calculate A_n. In order to evaluate the overall print quality of the model, the maximum print loss rate $\varphi_{\max} = \mathbf{max}_{n \in \mathbb{Z}_n}(\varphi_n)$ is chosen as the final print quality evaluation index, where $\mathbb{Z}_n$ is the set of member indexes in the model. The results of the print quality evaluation of the model with different minimum allowable self-supporting weight angles for Example 3 are shown in Table 5.

Table 5
Print quality evaluation of the model with different minimum allowable self-supporting angles in Example 3.

Minimum allowable self-supporting angles (°)	Measured diameter (mm)	Measured cross-sectional area A_i (mm^2)	Theoretical cross-sectional area A_0 (mm^2)	Maximum print loss rate φ_{max}
60	5.32	22.23	22.84	2.68%
50	3.90	11.95	13.12	8.95%
40	3.55	9.90	11.88	16.68%
30	2.37	4.41	10.58	58.31%

6. Print validation with WAAM

To demonstrate the versatility of our proposed framework across various AM configurations, this section presents a validation using WAAM. Similar to the FDM printing process, we initially determine the minimum self-supporting angle through an experiment with the trumpet-shaped model depicted in Fig. 10. This angle is then incorporated into Equations 1 and 2 to design a self-supporting truss structure. The final design is fabricated using a WAAM machine. For clarity, the entire framework is illustrated in the flowchart provided in Fig. 14.

The WAAM machine used in this study is illustrated in Fig. 15. It features a printing nozzle mounted on a KUKA robot arm, with a tiltable

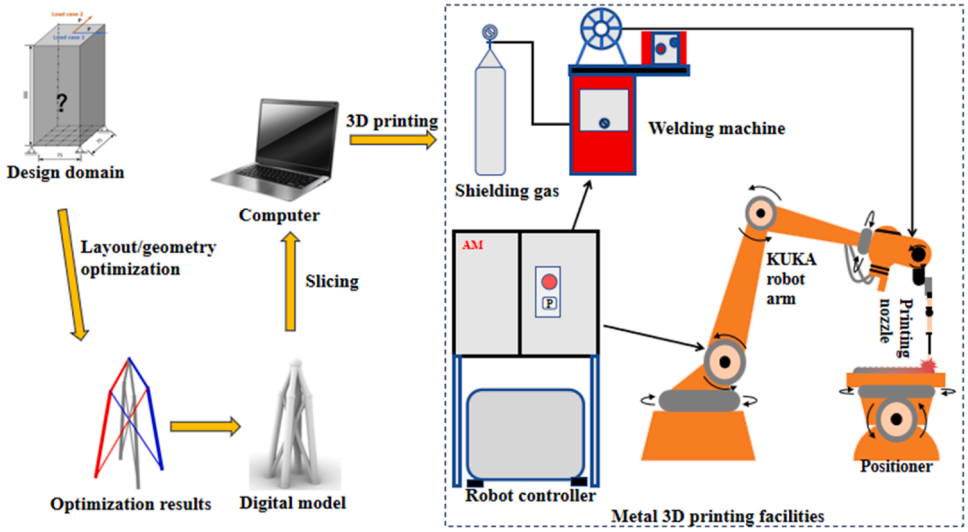

Fig. 14. Design and print process of self-supporting truss structures.

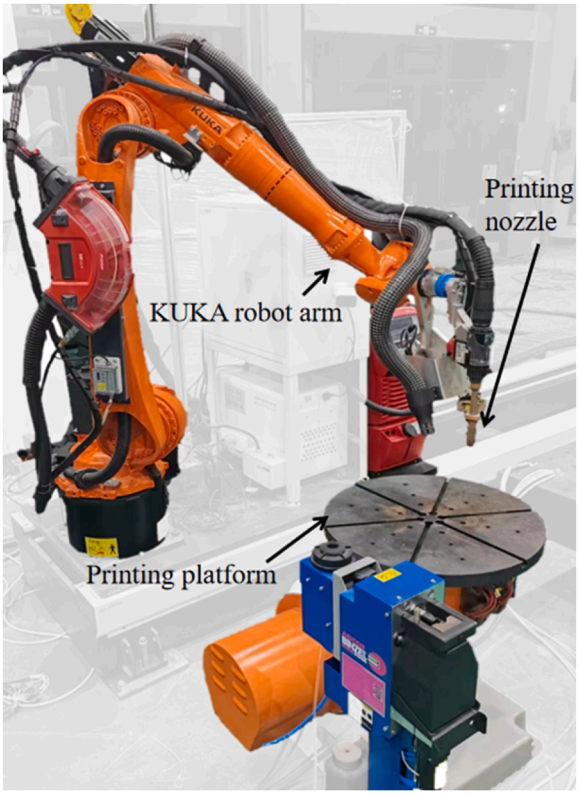

Fig. 15. WAAM machine with a KUKA robot arm and a tiltable platform.

platform positioned below. The specific parameters utilized in the printing process are detailed in Table 6. Using this equipment, we first designed a trumpet-shaped model in Rhino, featuring a bottom circle with 50 mm radius, a top circle with 170 mm radius, and a height of 120 mm. This model is then fabricated using the WAAM machine and the result is shown in Fig. 16. Carbon steel welding wire ER70S-6 was used as the feedstock material, and it was deposited onto a substrate plate made of Q235 steel grade. Due to the overhang effect, the printing process terminates at a height of 73 mm, suggesting a minimum self-supporting angle of 52°. This finding aligns closely with the reported values for directed energy deposition processes [41].

With the self-supporting angle obtained, a truss model of dimensions 75 mm × 75 mm× 300 mm (Fig. 17) is designed with the approach shown in Fig. 5. The self-supporting angle is conservatively set to 60°. A 1.2 mm bead height is used in the slicing process and the generated tool path is converted to KRL code that is compatible with the KUKA robotic arm. The successfully printed model shown in Fig. 18 demonstrates no defects caused by overhang, thus validating the effectiveness of the proposed framework applying in metal 3D printing of truss structures. However, it is noted that the WAAM process inherently has a larger self-supporting angle compared to the FDM process, leading to a compromise in material usage for optimization (see Table 4). To mitigate this, optimization techniques that account for the printing platform's rotatability could be leveraged [42,43].

7. Conclusion and discussion

This paper presents a framework that produces self-supportable and geometric-optimized designs for 3D printing. The overhang angles of the components are restricted during the layout and geometry procedures in the optimization process so that the optimized structure can be 3D printed without extra supporting materials. Based on the research in this paper, the following conclusions can be drawn:

(1) Geometry optimization can effectively reduce the number of redundant bars and nodes to simplify the layout without excessive material usage.
(2) Compared to the theoretical optimal solution, The increase in material consumption of the printable structure obtained by the optimization method in this paper is small. When the allowable self-supporting angle is set to 50°, the increase of material in the printed structures does not exceed 5% in this paper.

Table 6
WAAM printing parameters.

Print speed (m/min)	Wire feed rate (m/min)	Voltage (V)	Current (A)	Start current (A)	End current (A)	Rising time (s)	Falling time (s)	Temperature (℃)
0.01	4.8	14.6	160	168	80	0.1	0.3	360–380

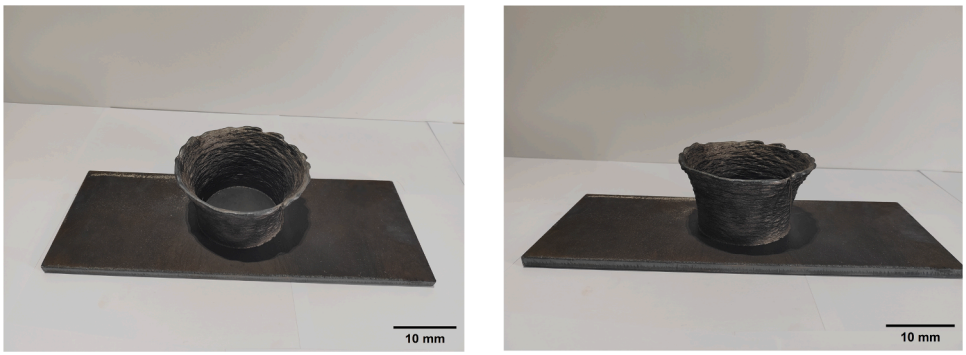

Fig. 16. Trumpet-shaped model used to determine the minimum allowable self-supporting angle in WAAM.

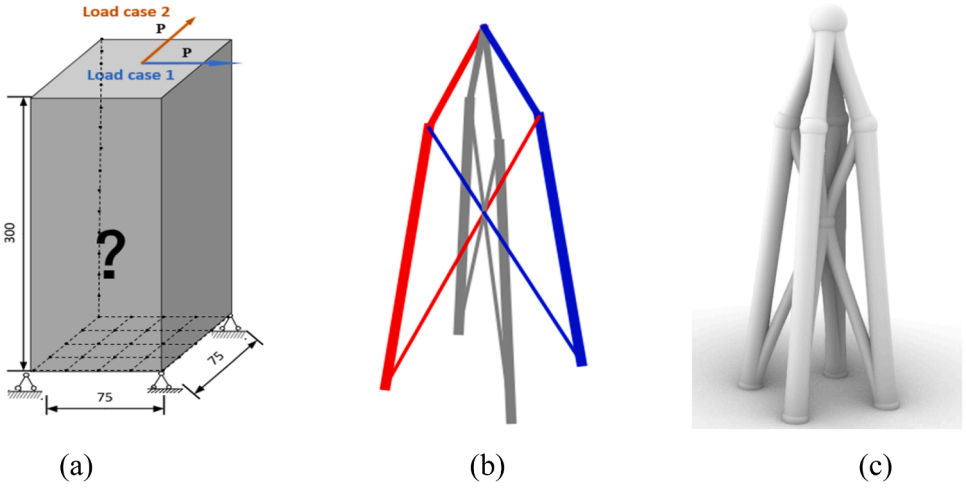

Fig. 17. Optimized truss structure for WAAM: (a) design domain; (b) optimization result; (c) physical model.

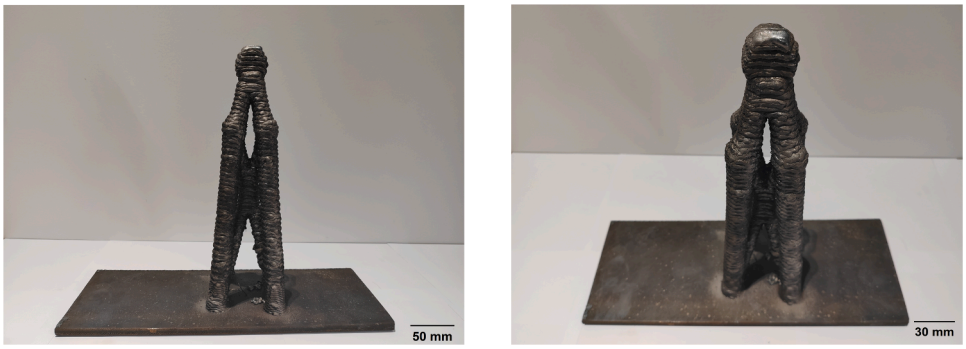

Fig. 18. An optimized truss structure printed by WAAM.

(3) When the minimum allowable self-supporting angle is not satisfied, the printing quality of the optimized structures cannot be ensured.
(4) The method outlined in this paper successfully generates self-supporting structures compatible with both FDM and WAAM printers, showcasing its remarkable adaptability across various additive manufacturing processes and materials.

Declaration of Competing Interest

The authors declare that they have no known competing financial interests or personal relationships that could have appeared to influence the work reported in this paper.

Acknowledgements

Finally, the authors would like to express their gratitude to the National Natural Science Foundation of China (Grant Number: 52208215), the Natural Science Foundation of Zhejiang Province (Grant Number: LQ22E080008) and The Center for Balance Architecture of Zhejiang University for their financial support for the work of this project.

References

[1] Liu J, et al. Current and future trends in topology optimization for additive manufacturing. Struct Multidiscip Optim 2018;57(6):2457–83.
[2] Gardner L, et al. Testing and initial verification of the world's first metal 3D printed bridge. J Constr Steel Res 2020;172:106233.

[3] Feucht T, et al. Additive manufacturing of a bridge in situ. Steel Constr 2022;15(2):100–10.
[4] Gardner L. Metal additive manufacturing in structural engineering–review, advances, opportunities and outlook. Structures 2023;47:2178–93.
[5] Huang C, et al. Mechanical testing and microstructural analysis of wire arc additively manufactured steels. Mater Des 2022;216:110544.
[6] Huang C, et al. Fatigue crack growth behaviour of wire arc additively manufactured steels. Int J Fatigue 2023;173:107705.
[7] Zhao Y, et al. Mechanical properties, microstructural characteristics and heat treatment effects of WAAM stainless-steel plate material. J Build Eng 2023:106988.
[8] Hadjipantelis N, Ben W, Gardner L. Characterisation of the anisotropic response of wire and arc additively manufactured stainless steel. ce/Pap 2021;4(2–4):1757–66.
[9] Laghi V, et al. Mechanical and microstructural features of wire-and-arc additively manufactured carbon steel thick plates. Int J Adv Manuf Technol 2023;127(3):1391–405.
[10] Huang C, Pinelopi K, Gardner L. Stress-strain curves for wire arc additively manufactured steels. Eng Struct 2023;279:115628.
[11] Guo X, et al. Experimental investigation of wire arc additively manufactured steel single-lap shear bolted connections. Thin-Walled Struct 2022;181:110029.
[12] Guo X, et al. Experimental study of DED-arc additively manufactured steel double-lap shear bolted connections. Eng Struct 2023;281:115736.
[13] Liu Y, et al. Experimental study on wire and arc additively manufactured steel double-shear bolted connections. J Build Eng 2023;76:107330.
[14] Li Z, Konstantinos D, Gardner L. A review of optimised additively manufactured steel connections for modular building systems. Ind Addit Manuf: Proc AMPA2020 2021:357–73.
[15] Huang C, Meng X, Gardner L. Cross-sectional behaviour of wire arc additively manufactured tubular beams. Eng Struct 2022;272:114922.
[16] Huang C, et al. Flexural buckling of wire arc additively manufactured tubular columns. J Struct Eng 2022;148(9):04022139.
[17] Zhang R, et al. Microstructure, mechanical properties and cross-sectional behaviour of additively manufactured stainless steel cylindrical shells. ce/Pap 2022;5(4):568–73.
[18] Meng X, et al. Optimisation and testing of wire arc additively manufactured steel stub columns. Thin-Walled Struct 2023;189:110857.
[19] Bruggi M, Laghi V, Trombetti T. Optimal design of wire-and-arc additively manufactured I-beams for prescribed deflection. Comput Assist Methods Eng Sci 2022;24(4):357–78.
[20] Laghi V, et al. Blended structural optimization for wire-and-arc additively manufactured beams. Prog Addit Manuf 2023;8(3):381–92.
[21] Feucht T, et al. Additive manufacturing by means of parametric robot programming. Constr Robot 2020;4:31–48.
[22] Dorn W, Gomory R, Greenberg H. Automatic design of optimal structures, Journal de. Mecanique 1964;3(1):25–52.
[23] Gilbert M, Tyas A. Layout optimization of large-scale pin-jointed frames. Eng Comput 2003;20(7/8):1044–64.
[24] Parkes EW. Joints in optimum frameworks. Int J Solids Struct 1975;11(9):1017–22.
[25] He L, Gilbert M. Rationalization of trusses generated via layout optimization. Struct Multidiscip Optim 2015;52(4):1–18.
[26] Smith CJ, et al. Application of layout optimization to the design of additively manufactured metallic components. Struct Multidiscip Optim 2016;54(5):1297–313.
[27] Jun Y, et al. An end-to-end framework for the additive manufacture of optimized tubular structures. IEEE Access 2021;9:165476–89.
[28] Liu Y, et al. Layout optimization of truss structures with modular constraints. Structures 2023;55.
[29] Zhu J., et al. Status and Future of Topology Optimization for Additive Manufacturing. Aeronautical Manufacturing Technology 2020; 63(10):15.
[30] Gaynor AT, et al. Topology optimization for additive manufacturing: considering maximum overhang constraint. 15th AIAA/ISSMO Multidiscip Anal Optim Conf 2014;2036.
[31] Gaynor AT, Guest JK. Topology optimization considering overhang constraints: eliminating sacrificial support material in additive manufacturing through design. Struct Multidiscip Optim 2016;54(5):1157–72.
[32] Langelaar M. An additive manufacturing filter for topology optimization of print-ready designs. Struct Multidiscip Optim 2017;55:871–83.
[33] Qian X. Undercut and overhang angle control in topology optimization: a density gradient based integral approach. Int J Numer Methods Eng 2017;111(3):247–72.
[34] Zhang W, Lu Z. Topology optimization of self-supporting structures with polygon features for additive manufacturing. Comput Methods Appl Mech Eng 2018;334:56–78.
[35] Kuo Y, Cheng C. Self-supporting structure design for additive manufacturing by using a logistic aggregate function. Struct Multidiscip Optim 2019;60:1109–21.
[36] Zhao D, Li M, Liu Y. A novel application framework for self-supporting topology optimization. Vis Comput 2021;37:1169–84.
[37] He L, et al. Conceptual design of AM components using layout and geometry optimization. Comput Math Appl 2019;78(7):2308–24.
[38] Michell AG. LVIII. The limits of economy of material in frame-structures. Lond, Edinb, Dublin Philos Mag J Sci 1904;8(47):589–97.
[39] Rhinoceros 7, https://www.rhino3d.com/, 2021.
[40] Repetier-Host version 0.90, https://www.repetier.com/, 2018.
[41] Nassar, A.R. and Reutzel, E.W. Beyond Laser-by-Laser Additive Manufacturing-Voxel-Wise Directed Energy Deposition. In 2014 International Solid Freeform Fabrication Symposium.
[42] Lu H, He L, Gilbert M, Gilardi F, Jun Y. Design of optimal truss components for fabrication via multi-axis additive manufacturing. Comput Methods Appl Mech Eng 2024;418:116464.
[43] Jun Y, Guo Q, Lu H, Kyvelou P, Zhao Y, Gardner L, et al. Topology optimisation of self-supporting structures based on the multi-directional additive manufacturing technique. Virtual Phys Prototyp 2023;18(1):2271458.